2006

Non-equilibrium ionization model for stellar cluster winds and its application

L Ji

QD Wang
University of Massachusetts - Amherst

J Kwan

NON-EQUILIBRIUM IONIZATION MODEL FOR STELLAR CLUSTER WINDS AND ITS APPLICATION

Li Ji, Q. Daniel Wang, and John Kwan

Department of Astronomy, University of Massachusetts, Amherst, MA 01003-9305;
ji@nova.astro.umass.edu, wqd@astro.umass.edu, and kwan@nova.astro.umass.edu

ABSTRACT

We have developed a self-consistent physical model for super stellar cluster winds based on combining a 1-D steady-state adiabatic wind solution and a non-equilibrium ionization calculation. Comparing with the case of collisional ionization equilibrium, we find that the non-equilibrium ionization effect is significant in the regime of a high ratio of energy to mass input rate and manifests in a stronger soft X-ray flux in the inner region of the star cluster. Implementing the model in X-ray data analysis softwares (e.g., XSPEC) directly facilitates comparisons with X-ray observations. Physical quantities such as the mass and energy input rates of stellar winds can be estimated by fitting observed X-ray spectra. The fitted parameters may then be compared with independent measurements from other wavelengths. Applying our model to the star cluster NGC 3603, we find that the wind accounts for no more than 50% of the total "diffuse" emission, and the derived mass input rate and terminal velocity are comparable to other empirical estimates. The remaining emission most likely originate from numerous low-mass pre-main-sequence stellar objects.

Subject headings: atomic processes —plasmas — stars: winds, outflows — open clusters and associations: individual: NGC 3603 — X-ray: general

1. INTRODUCTION

Super star clusters (SSCs) consist of densely-packed massive stars with typical ages of a few Myr. They are the most energetic coeval stellar systems, identified in a wide range of star-forming galaxies (Whitmore 2000). Within a characteristic radius of a few pc or less, winds from individual stars in such a cluster are expected to collide and merge into a so-called stellar cluster wind. In some extragalactic systems, such as the nuclear region of M82 (Strickland et al. 2002), winds from star clusters, either individually or collectively, can be energetic enough to drive galaxy-scale superwinds. Consequently, cluster winds can play an important role in shaping star formation and galaxy evolution in general (Heckman et al. 1990).

Observationally, X-ray emission that appears to be diffuse has been detected around star clusters (e.g., NGC 3603, Moffat et al. 2002; Arches cluster at the Galactic center, Yusef-Zaden

et al. 2002, Rockefeller et al. 2005, Wang et al. 2006). Theoretically, both stellar cluster wind (e.g., Stevens & Hartwell 2003, and references therein) and galactic superwind (e.g., Strickland & Stevens 1999; Breitschwerdt & Schmutzler 1999) have been investigated, particularly in terms of their expected X-ray luminosities. However, neither the observed spectral nor spatial information has been used to confront the theoretical model prediction quantitatively. Furthermore, most models assume collisional ionization equilibrium (CIE) and no non-equilibrium ionization (NEI) model is available for a quantitative comparison with current X-ray data of stellar cluster winds and/or superwinds.

In this paper, we first introduce our non-equilibrium ionization model for stellar cluster winds based on combining a 1-D steady-state adiabatic wind solution (§2) with a non-equilibrium ionization calculation (§3). The non-equilibrium ionization effect is examined within a grid of parameter space, which is described in §4. Then we report its application to the diffuse X-ray emission of NGC 3603 (§5). The physical parameters (e.g., mass input rate, terminal velocity, and metallicity) of the stellar cluster wind are derived from the fits and compared with other independent measurements and empirical estimates.

2. X-RAY EMISSION FROM STELLAR CLUSTER WINDS

On the scale of a galaxy, supernovae in a starburst region can drive a strong wind. Chevalier & Clegg (1985) describe it by an outflow model with uniformly distributed mass and energy depositions within a radius. Their solutions are scalable to the case of a star cluster, in which the mass loading and energy input are due to stellar winds instead of supernovae.

Essentially analogous to the model of Chevalier & Clegg (1985), Cantó, Raga & Rodríguez (2000) present an analytic 1-D model to describe the cluster wind. In addition, their 3-D numerical simulation of stellar winds from 30 stars produces a mean flow that agrees well with their analytic model. They predict that the X-ray emission from the cluster wind of the Arches cluster (see also Raga et al. 2001) is detectable (Law & Yusef-Zadeh 2004). Also based on the work of Chevalier & Clegg (1985), Stevens & Hartwell (2003, henceforth, SH03) present a model that allows for a lower energy transfer efficiency and mass loading. This model predicts global properties such as the X-ray luminosity and gas temperature at an individual cluster center. A crude comparison of the model predictions and existing *Chandra* observations does not give any conclusive result as to whether or not the diffuse emission is genuinely associated with cluster winds.

All of the above theoretical models assume CIE for the ionization structure. However, one may suspect that the gas in a cluster wind may be in a highly NEI state, because of both the rapid shock heating in the wind-wind collision and the fast adiabatic cooling in the subsequent expansion. Fig. 1 illustrates such a NEI condition in a cluster wind. Clearly, the dynamic (adiabatic) cooling time scale defined by $T/(dT/dt)$ is much shorter than the recombination time scales of all key ion species, and CIE does not hold.
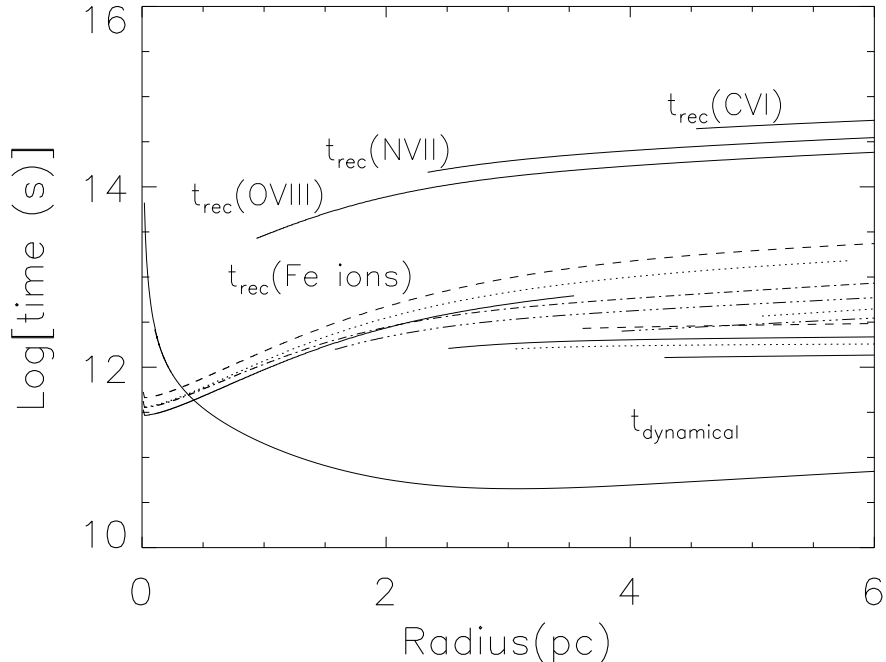
Fig. 1.— Dynamical timescale compared with intrinsic recombination timescales for a 1-D cluster wind with an exponentially distributed mass input rate $\dot{M}_0 = 2.3 \times 10^{-4}$ M$_\odot$ yr^{-1}, a terminal velocity $V_\infty = 2000$ km s^{-1}, and a sonic radius $r_s = 1.38$ pc.

Moreover, the mass and energy injections in the previous theoretical models are input parameters and are crudely estimated from the properties (e.g., spectral type and radio flux) of individual massive cluster stars. Such a modeling approach suffers significant uncertainties and has little predictive power. Stellar mass loss remains one of the largest uncertainties in stellar evolution (e.g., Kudritzki & Puls 2000). Massive stars are also not the only sources of mass loss; other cold mass loading, such as outflows from protostars(e.g., SH03), may also be important.

In the following subsections, we introduce our dynamic model of a stellar cluster wind.

2.1. Cluster Wind Dynamics

We consider a young star cluster (age $\leq 5 \times 10^6$ yrs), from which the main mass and energy injections are due to stellar winds, especially from those massive OB and Wolf-Rayet stars. Extending SH03's work, which assumes a uniform distribution of stars, we have constructed a 1-D steady-state wind model with (1) either an exponential or uniform distribution of stars; (2) a steady and spherically symmetric cluster wind; (3) mass and energy injections following the stellar mass distribution; (4) gravity and radiative cooling being neglected. This cluster wind can then be

described by the following steady-state Euler equations:

$$\frac{1}{r^2}\frac{d}{dr}(\rho u r^2) = \dot{m}(r) \tag{1}$$

$$\rho u \frac{du}{dr} = -\frac{dP}{dr} - \dot{m}(r)u \tag{2}$$

$$\frac{1}{r^2}\frac{d}{dr}\left[\rho u r^2(\frac{1}{2}u^2 + \frac{\gamma}{\gamma-1}\frac{P}{\rho})\right] = \dot{E}(r) \tag{3}$$

where u, ρ and P are the velocity, density and pressure of the flow respectively, and γ is the adiabatic index, taken as 5/3 for an ideal gas, while $\dot{m}(r)$ and $\dot{E}(r)$ are the mass and energy input rates per unit volume and are assumed to be proportional to the stellar mass density $\rho_s(r)$.

The total mass and energy input rates are $\int_0^\infty 4\pi r^2 \dot{m}\,dr = \dot{M}_0$ and $\int_0^\infty 4\pi r^2 \dot{E}\,dr = \dot{E}_0$. When the stellar mass distribution is assumed to be uniform, $\dot{M}_0 = \frac{4}{3}\pi r_c^3 \dot{m}$ and $\dot{E}_0 = \frac{4}{3}\pi r_c^3 \dot{E}$, where r_c is the cluster radius, which coincides with the sonic radius; the analytic solutions of Eq. (1)-(3) can be found in Chevalier & Clegg (1985). For an exponential stellar mass distribution, $\rho_s(r) \propto exp(-r/r_{sc})$, where r_{sc} is the scale radius. We solve the above Euler equations numerically. Because gravity is negligible, the sonic radius depends on the stellar mass distribution alone.

The above hydrodynamical equations do not predict how the electron temperature changes in the cluster. The temperature depends on how the electron is heated. We consider two extreme cases: one that has the electron and ion temperatures in equilibration, i.e., $T_e = T_i = T$; the other that sets the initial $T_e/T = 10^{-3}$ and lets the ratio evolve via electron-ion Coulomb collisions. Here, the mean temperature $T \equiv (\mu m_p/k)P/\rho$ and μ is the mean mass per particle in terms of the proton mass m_p. Assuming cosmic abundances, the variation in the electron temperature follows the equation (e.g., Eq. (1) in Borkowski et al. 1994):

$$\frac{d(T_e/T)}{dt} = 1.2 \times 10^{-4} n(\frac{T}{10^7 K})^{-3/2}(\frac{T_e}{T})^{-3/2}(1 - \frac{T_e}{T}) \text{ yr}^{-1}, \tag{4}$$

where n is the total particle number density.

Our model has four parameters: mass input rate $\dot{M}_0$, stellar wind terminal velocity V_∞ (assuming $\dot{E}_0 = 1/2\dot{M}_0 V_\infty^2$), abundance Z, and the scale radius r_{sc} (or cluster radius r_c for a uniformly mass distributed model). Fig. 2 illustrates the radial profiles of the mean/electron temperature, density, terminal velocity and mass input rate for these two stellar distribution models with the same sonic radius. Two sonic radii (0.69 pc, black; 1.38 pc, green) are considered here. When the sonic radius is larger, the density is lower in the inner part of the cluster, the temperature drops more slowly, and the terminal velocity of the wind is reached at a larger radius.
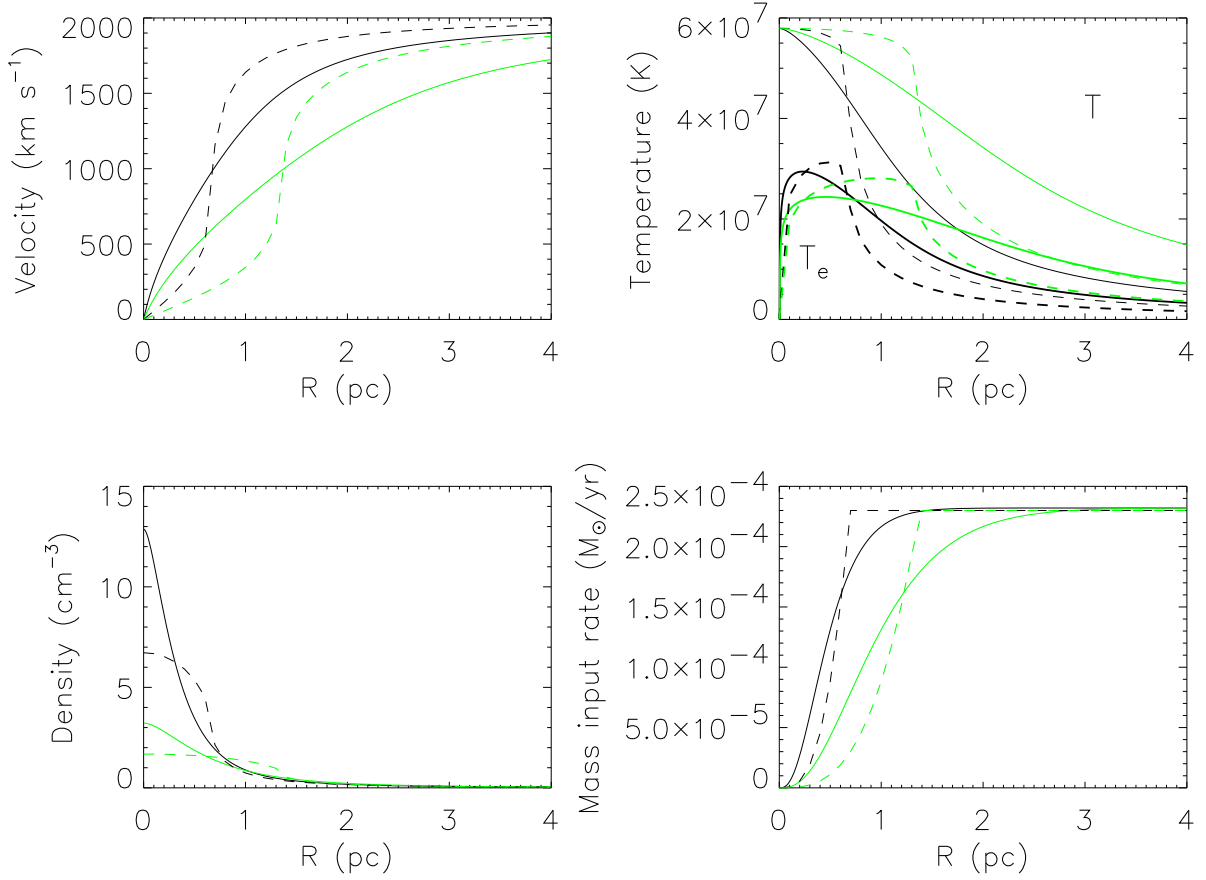
Fig. 2.— The radial profiles of the cluster wind (solid line — exponential distribution; dash line — uniform distribution) the velocity (top left panel), mean temperature (T, top right, thin lines), electron temperature (T_e, top right, thick lines), density (bottom left), and cumulative mass input rate (bottom right). Two models with different sonic radii (0.69 pc, black; 1.38 pc, green) are shown for each stellar mass distribution. The same mass input rate $\dot{M}_0 = 2.3 \times 10^{-4}$ M$_\odot$ yr^{-1} and stellar wind terminal velocity $V_\infty = 2000$ km s^{-1} are assumed.

2.2. X-ray Emission Calculation

The broad band X-ray luminosity L_X of the cluster wind within a region ($r < R$) is given by:

$$L_X = \int_0^R 4\pi r^2 n_e n_h \int_X \Lambda_\nu d\nu \; dr \tag{5}$$

where X is the frequency band of interest; n_e and n_h are the electron and hydrogen number density respectively; Λ_ν is the specific emissivity at frequency ν, and the cluster wind is assumed to be optically thin. Generally Λ_ν is a function of elemental abundances, local ionic fractions and electron temperature.

The model-predicted spectrum S_ν from a given projected annulus between the inner-to-outer radii $[R_{in}, R_{out}]$ can be calculated using the following equation:

$$S_\nu(R_{in}, R_{out}) = \frac{1}{D^2} \int_{R_{in}}^{R_{out}} 2\pi R dR \int_R^\infty \frac{2n_e(r)n_h(r)\Lambda_\nu r}{\sqrt{r^2 - R^2}} dr, \tag{6}$$

where D is the distance to the cluster. The observed surface brightness can be predicted as:

$$\Sigma_X(R) = \frac{1}{4\pi} \int_R^\infty \frac{2n_e(r)n_h(r)r}{\sqrt{r^2 - R^2}} \int_X \int_{X'} \Lambda_{\nu'} A(\nu') E(\nu', \nu) d\nu' d\nu dr \tag{7}$$

where $A(\nu')$ and $E(\nu', \nu)$ are the on-axis effective area and energy response matrix of the X-ray telescope/instrument.

In principle, both the spatial and spectral information of the data can be used to constrain our model. But while we may reasonably assume the spectrum of the undetectable point sources to be the same as that of detected point sources, a similar assumption about the surface brightness cannot be made because the detected point sources are sparse and incomplete in a typical observation. Therefore, unlike the spectrum, the observed surface brightness cannot easily be compared with the model prediction at present.

3. NON-EQUILIBRIUM IONIZATION SPECTRAL MODEL

In the past, NEI models have been developed for (1) time-dependent isobaric or isochronic cooling of shock-heated gas (e.g., Sutherland & Dopita 1993), (2) delayed ionization in SNRs (e.g., Borkowski et al. 2001), and (3) delayed recombination in galactic winds (e.g., Breitschwerdt & Schmutzler 1999) or in the Local Bubble (e.g., Breitschwerdt et al. 1996). The atomic data used are typically more than a decade old and are stored in a way that is difficult to update. Moreover, the physical processes included are not complete, due to either the lack of atomic data or the use of the CIE approximation. One example of such a process is the cascade of electrons following recombinations into highly excited levels, which could strongly affect the line emissivities of highly ionized species (e.g., Gu 2003).

We have developed a NEI spectral model that has the following characteristics: (1) the ionization code is separated from the atomic data so that the latter can be updated conveniently; (2) the most updated atomic data are used; (3) recombinations into highly excited levels are included; (4) the electron temperature evolution, the dynamics, and the ionization structure are determined self-consistently.

3.1. Atomic Data

Our atomic data are based on CHIANTI (Young et al. 2003, version 4.2), which provides a database of atomic energy levels, transition wavelengths, radiative transition probabilities (A-rates)

and electron collisional excitation rates for 23 elements from H ($Z = 1$) to Zn ($Z = 30$), totally 206 ions.

Spectral calculations involving detailed fine structure levels are time-consuming and are not necessary for the current X-ray CCD spectral resolution. Therefore, we have combined those fine structure levels together according to their degeneracies and have re-calculated the collisional excitation rates and A-rates. For example, for the hydrogen ion there are totally 25 energy levels listed in CHIANTI. After regrouping, we get six principle energy levels (1s, 2s, 2p, n=3, n=4 and n=5). For n=3, there are five sub-levels ($j = 3s$, $3p_{1/2}$, $3p_{3/2}$, $3d_{3/2}$, and $3d_{5/2}$), which we regroup as one. The new collisional de-excitation rate and A-rate are $C_{3,i} = \sum_j \frac{g_j}{g} C_{3j,i}$ and $A_{3,i} = \sum_j \frac{g_j}{g} A_{3j,i}$ respectively, where g_j is the individual sub-level degeneracy and g is the total.

A comparison between CHIANTI and our code with the regrouped data is shown in Fig. 3. The total luminosity difference between the two spectra is less than 1%. The difference in the line structure is very slight at $\gtrsim 0.5$ keV and somewhat more noticeable at lower energies. But such difference is well within the uncertainties of the atomic data.
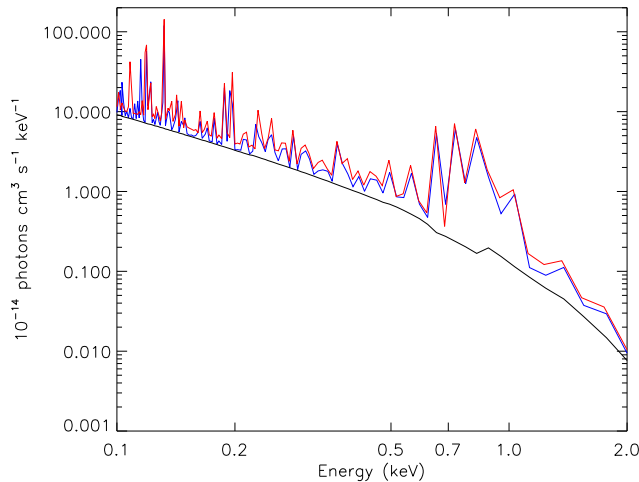

Fig. 3.— Comparison between the CIE spectra of CHIANTI (blue) and our code with regrouped atomic data (red), assuming $T = 5 \times 10^6$ K, cosmic abundance given by Allen (1973), and the ion fractions from Mazzotta et al. (1998). The black line denotes continuum. A spectrum bin size of 1Å is used.

The ionization structure of a plasma is determined by the collisional ionization and radiative and dielectronic recombinations (e.g., Mazzotta et al. 1998, and references therein). CHIANTI does not offer the rates of these atomic processes. We have taken the collisional ionization cross-sections from Arnaud & Rothenflug (1985) and Arnaud & Raymond (1992), and radiative and dielectronic recombination rates from Verner & Ferland (1996) and Mazzotta et al. (1998), except for Carbon, Nitrogen and Oxygen. For these three species, we use the results of Nahar (2000), based on a large-scale close-coupling R-matrix calculation for photoionization cross-sections and

recombination coefficients. We assume that three-body recombinations are not important at the density range under consideration and neglect them for all ions. Our current code also does not include charge-exchange reactions.

Fig. 4 compares the CIE ionic fractions of our calculation with those given by Mazzotta et al. (1998, henceforth Mazz98). All, except for C, N, O and Fe, agree well because the same atomic data are used. We find good agreement for all the ions of N, with the difference being less than 10%. For C and O, there is good agreement except for CV, CVI, OIV, OV and OVI, for which the difference can reach up to 50% near the peak of maximum ionic fraction. For example, at $T \approx 2 \times 10^5$K, our ionic fraction of OV is a factor of two less than that of Mazz98. From $T \approx 3 \times 10^6$ K to $T \approx 1.5 \times 10^7$ K where ionic fractions of Fe XV to Fe XXI are significant, our calculation is substantially different from Mazz98, particularly for FeXVII to FeXXII. This is due to different radiative recombination rates employed.
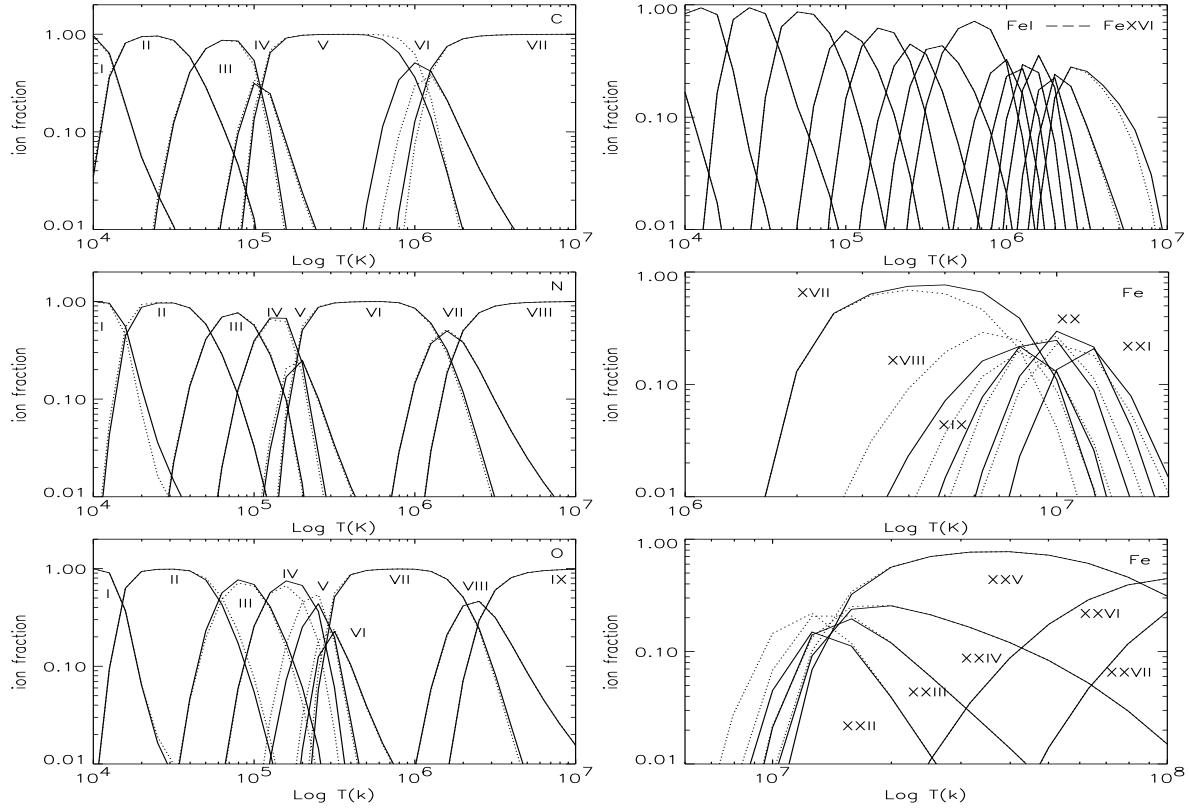

Fig. 4.— CIE ion fractions of our model (solid) and Mozz98's (dotted) for elements C, N, O, and Fe as marked in individual panels.

3.2.   Continuum and Line Emissions

The continuum emission consists of free-free, free-bound and two-photon continua. We include two important two-photon transitions: H-like $2s \rightarrow 1s$ and He-like $1s2s^1S_0 \rightarrow 1s^2\ ^1S_0$.

There are several ways to produce spectral lines in a plasma. Most spectral lines are produced by electron collisional excitation of ions followed by the radiative decay of the excited level. At X-ray energies free electrons can also excite an inner-shell electron to a level above the ionization potential. The excited level of the ion then undergoes either a radiative decay to a lower energy level to produce a satellite line, or an autoionizing transition to the next ionization stage (Dere et al. 2001). We follow CHIANTI in treating this autoionizing transition as a radiative decay to the ground level but with no emission of radiation. In addition, we include the line emission following an inner-shell ionization. For example, an impact ionization from the inner $1s^2$ shell of ion $Z^{+(z-1)}$ contributes to the production of a certain line in the next higher ion Z^{+z}. We use the database of Mewe & Cronenschild (1981) for such lines (see Gorczyca et al. (2003) for an assessment of the database accuracy).

Line photons are also produced during the cascade following a radiative recombination into an excited level. This process is particularly important in a delayed recombination scenario. A dielectronic recombination leads to the capture of an incident electron into an excited state above the ionization threshhold of the recombined ion and also emits a photon if an autoionization does not ensue.

3.3.   Level Balance Equations

Electron populations at various energy levels of each ion are determined by such processes as collision excitation/de-excitation and radiative decay; the level balance equations are:

$$n_i \sum_{j \neq i} \alpha_{ij} = \sum_{j \neq i} n_j \alpha_{ji}, \tag{8}$$

where i and j denote individual levels of an ion, α_{ji} is the total rate of the transitions between the two levels, and n_i is the level i population relative to the total level population.

In a low density plasma, collisional excitation generally dominates over recombination in populating the excited states. In an over-cooled NEI state, however, the temperature may be sufficiently low that recombination can make a non-negligible contribution to the level population (e.g., Dere et al. 2001). We include radiative recombinations into the principle energy levels ($n = 1$ to 6) of each ion; the level balance equation for ion Z^{+z} (element Z with z electrons removed) is

$$n_i \sum_{j \neq i} \alpha_{ij} = \sum_{j \neq i} n_j \alpha_{ji} + n_{\mathrm{e}} \frac{N(Z^{+(z+1)})}{N(Z^{+z})} RR(Z^{+(z+1)})_i \tag{9}$$

$$= n_j(n_{\rm e}C_{ji} + A_{ji}) + n_{\rm e}\frac{N(Z^{+(z+1)})}{N(Z^{+z})}RR(Z^{+(z+1)})_i \tag{10}$$

where C_{ji} is the electron collisional rate, A_{ji} is the radiative decay rate (zero if $j < i$), and $RR(Z^{+(z+1)})_i$ is the radiative recombination rate to the level i of ion $Z^{+(z)}$. Following Osterbrock (1989), we calculate the rate using Milne's relation and the photoionization cross sections of Karzas & Latter (1961) for excited states and those of Verner & Yakovlev (1995) for ground states. Thus,

$$RR(Z^{+(z+1)})_i = \int_\nu \alpha_{\nu,i}d\nu, \tag{11}$$

and

$$\alpha_{\nu,i} = \frac{4}{\sqrt{\pi}}\frac{g_i}{g_{z+1}}\frac{h^3\nu^2}{c^2(2m_ekT)^{3/2}}e^{-h(\nu-\nu_T)/kT}\sigma_{phot,i}(\nu) \tag{12}$$

where g_i and $\sigma_{phot,i}$ are the degeneracy and photoionization cross section of level i of ion $Z^{+(z)}$.

3.4. Non-equilibrium Ionization Calculations

In general the dynamics and ionization of a plasma are entangled. The ionization structure, through its heating/cooling effects, can affect the temperature evolution. However, in a cluster wind, radiative cooling can typically be neglected and the dynamics and ionization of the wind can be separated. With the mass input having a certain spatial distribution in our model, and assuming the newly injected gas to be neutral, the cluster wind number density of the neutral ion $N_{Z,0}$ for a given element Z evolves in a cluster wind as:

$$\frac{1}{r^2}\frac{dN_{Z,0}ur^2}{dr} = \frac{Z\dot{m}(r)}{m_Z} - n_eN_{Z,0}S_{Z,0} + n_eN_{Z,1}\alpha_{Z,1}, \tag{13}$$

with Z and m_Z being the abundance and mass of element Z.

The number density of other ions $(N_{Z,z>0})$ of the same element will follow:

$$\frac{1}{n_e}\frac{dN_{Z,z>0}}{dt} = N_{Z,z-1}S_{Z,z-1} - N_{Z,z}(S_{Z,z} + \alpha_{Z,z}) + N_{Z,z+1}\alpha_{Z,z+1}, \tag{14}$$

where $S_{Z,z}$ and $\alpha_{Z,z}$ are the total ionization ($z \rightarrow z+1$) and recombination ($z \rightarrow z-1$) rate coefficients (in cm^3 s^{-1}) of ion Z^{+z}. Our interest here is in highly ionized ions. Therefore, the exact ionization state of the injected gas is not important as long as it is cold or warm (i.e. $T \lesssim 10^4$ K).

For each element, we simultaneously solve these differential equations using IDL code LSODE which adaptively solves stiff and non-stiff systems of ordinary differential equations.

In an evolving plasma, a characteristic time scale to approach a CIE state is $\tau_{CIE} \approx [n_e(S_{Z,z} + \alpha_{Z,z})]^{-1}$ (Mewe 1997). The CIE approximation requires the cooling/heating time be much longer

than τ_{CIE}. As mentioned earlier, CIE is only a special case. If experiencing a rapid heating or cooling process such as thermal instability, shock, or rapid expansion, a plasma may be under-ionized or over-ionized, compared to the CIE result (Dopita et al. 2002).

As an illustration, we consider a toy model for an adiabatically expanding stellar cluster wind with a constant mass input rate $\dot{M} \sim 3 \times 10^{-5}$ M$_\odot$ yr^{-1} and a constant velocity $v = 1000$ kms^{-1}. We assume that the wind is injected at an initial radius of $r_0 = 0.3$ pc and is heated up to a CIE state with an equilibrium temperature $T_0 = 5 \times 10^6$ K. As the wind expands adiabatically, its temperature drops as $T = T_0(r/r_0)^{-4/3}$. Fig. 5 compares the CIE and non-CIE spectra at $r = 1$ pc, where $T \sim 1 \times 10^6$ K (left panel) and at $r = 2$ pc, where $T \sim 4 \times 10^5$ K (right panel). The difference is significant: in the lower energy part, the line intensities in the non-CIE spectrum are weaker than those in the CIE case, while in the upper energy part saw-tooth structures are present in the non-CIE spectra; all these are due to delayed recombinations. Fig. 6 shows the spectra at
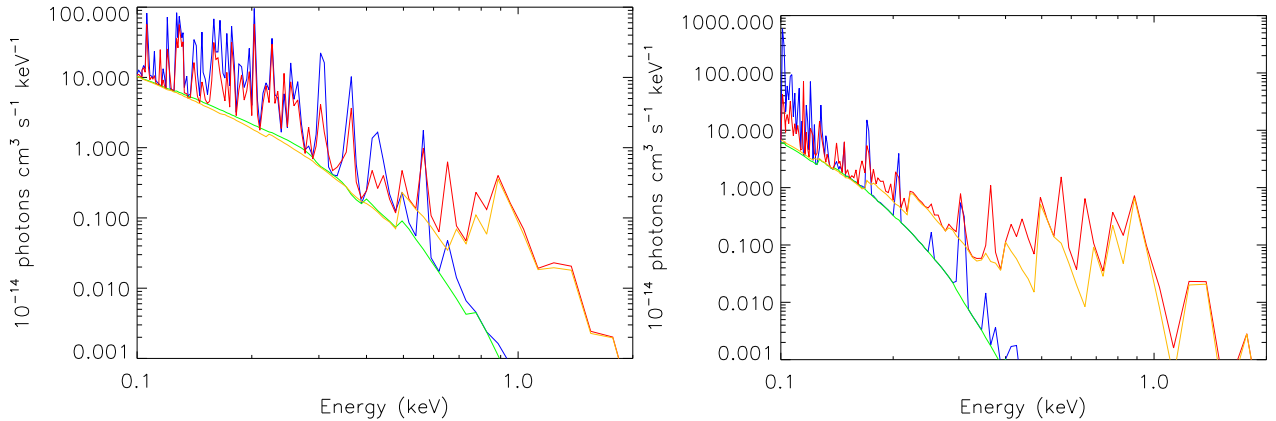

Fig. 5.— Spectra of an adiabatically expanding cluster wind at $r = 1$ pc (left panel) and 2 pc (right panel): CIE (total — blue line; continuum only — green line) and non-CIE (total — red line; continuum only — yellow line) calculations.

the same two radii with and without including the cascade of electrons following recombinations to $n > 1$ levels. The cascade lines of CV, CVI, OVII and OVIII are clearly visible.

The more general model for a cluster wind with distributed mass and energy injections has been described in §2.1, and the radial profiles of the wind are shown in Fig. 2. We use the case of $\dot{M}_0 = 2.3 \times 10^{-4}$ M$_\odot$ yr^{-1}, $V_\infty = 2000$ km s^{-1}, and a sonic radius $r_s = 1.38$ pc to illustrate the effect of a distributed mass injection on the ionization structure. Fig. 7 compares the ionic fractions of C, N, O and Fe at four radii between the case in which $\dot{M}_0$ is all injected at the center and that in which it is injected in an exponential distribution. The effect of the distributed mass injection clearly shows up as a long ionization tail.
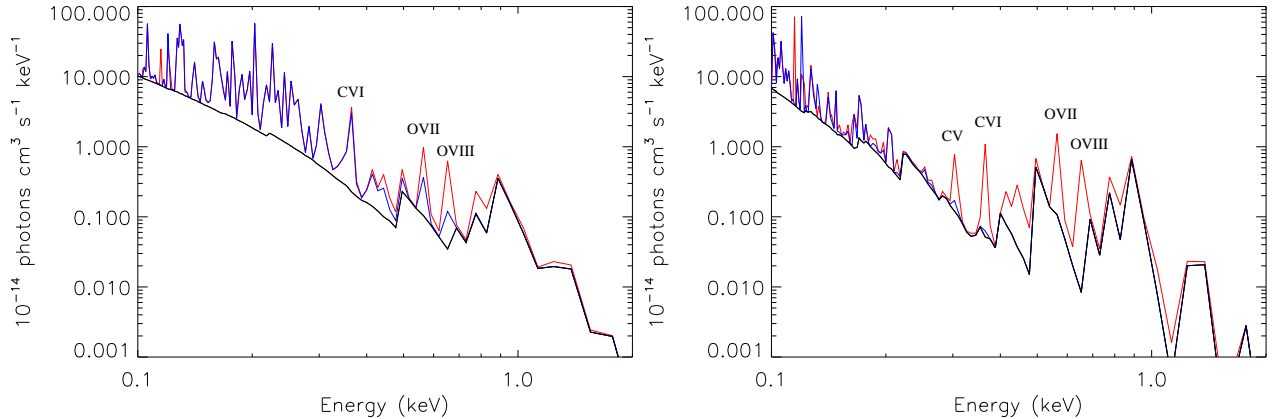
Fig. 6.— Spectra with (red) and without (blue) adding the cascades following radiative recombinations to highly excited levels for an adiabatically expanding stellar cluster wind (see text for details). Black line denotes continuum only.

4. MODEL PREDICTIONS FOR STELLAR CLUSTER WINDS

To illustrate the condition under which the NEI effect is significant for stellar cluster winds, we here consider a cluster of an exponential stellar distribution with a scale radius $r_{sc} = 0.48$ pc, corresponding to a sonic radius at $R_s = 1.97$ pc. We calculate results for a parameter grid: $\dot{M}_0 = 10^{-4}$ and 10^{-3} $M_\odot$ yr^{-1}; $V_\infty = 500, 1000,$ and 2000 km s^{-1}. The velocity, temperature, and density profiles of the wind are illustrated in Fig. 8. We consider both the equilibration and non-equilibration cases of the electron and ion temperatures (§2.1) and both the CIE and non-CIE scenarios for comparison. To demonstrate the results, we calculate the intrinsic cumulative spectra for three annular regions, $[0, R_s]$, $[R_s, 2R_s]$, and $[2R_s, 4R_s]$, as well as the predicted *Chandra* ASIS-S count intensity distribution over the $[0, 2R_s]$ range and in two energy bands, $[0.3, 2.0]$ keV and $[2.0, 8.0]$ keV. For illustration, we assume that the distance to the cluster is $D = 10$ kpc and that the metal abundance is solar.

First, we find that the separate T_e evolution does not lead to significant spectral difference in the cumulative spectrum. It is already seen from Fig. 8 that T_e is significantly lower than T only when the density is low (i.e. $V_\infty = 2000$ km s^{-1} and $\dot{M}_0 = 10^{-4}$ $M_\odot$ yr^{-1}). Even in this case the ionic fractions of the key O and Fe ions are fairly similar (Fig. 9). The biggest difference in the ionic fractions between the two T_e evolutions occurs during the rise of T_e from 10^5 K to 10^7 K in the non-equilibration evolution ($R \lesssim 0.01 R_s$). In the region making the most contribution to the X-ray flux ($2R_s \gtrsim R \gtrsim 0.05 R_s$), the ionic fractions are comparable between the two T_e evolutions in either the CIE or non-CIE case. Henceforth in the following discussions on the cumulative spectrum and count intensity distribution, only the results from the T_e evolution via Coulomb interactions are used.

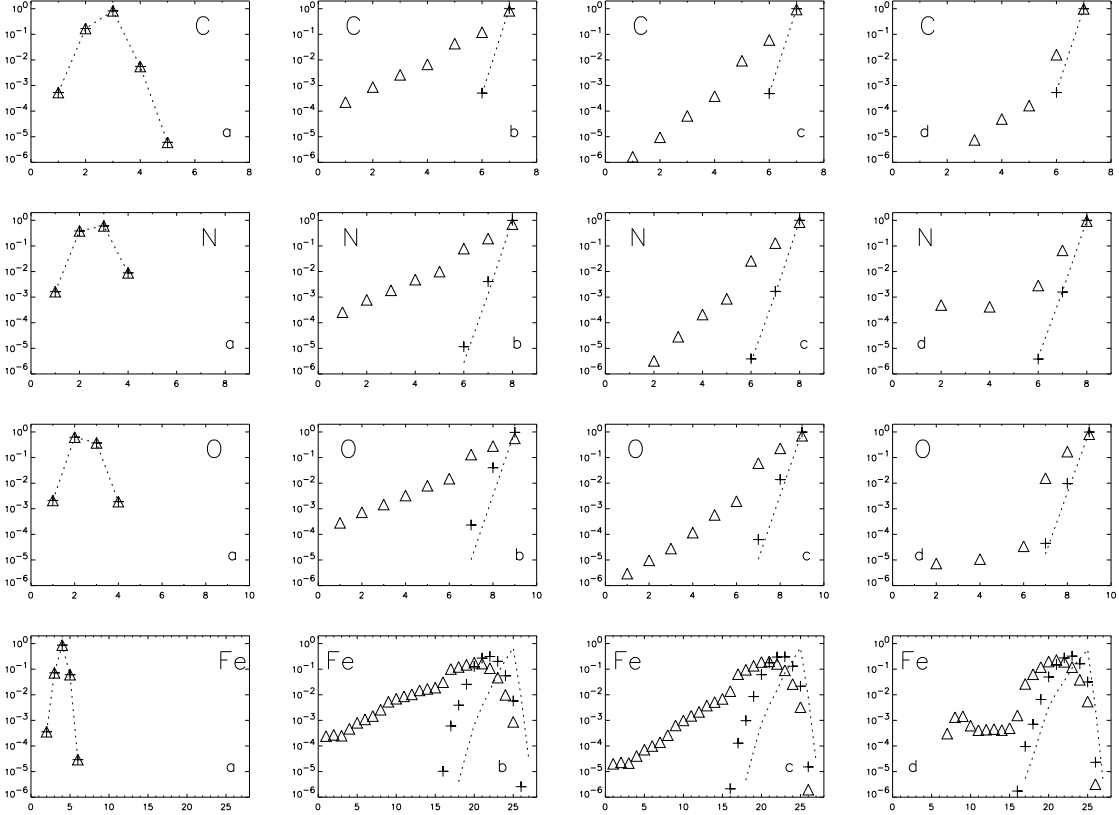Second, we find that the effect of the NEI manifests itself in both the inner and outer regions

Fig. 7.— C, N, O and Fe ion fractions calculated for a cluster wind at four radii: panel a (0.003 pc), b (0.30 pc), c (0.72 pc) and d (1.38 pc). Two mass injection scenarios are assumed: all at the center (crosses, and the dotted lines denote the corresponding CIE calculation) and in an exponential distribution (triangle). Y-axis denotes the ion fraction, X-axis denotes the ionic stage (e.g., 1 denotes I).

of the cluster wind, but under different dynamical conditions. In the inner region it is expected that the CIE and non-CIE calculations will be similar for the cases of high central densities. Fig. 10 illustrates such a case ($\dot{M}_0 = 1 \times 10^{-4}$ M$_\odot$ yr^{-1} and $V_\infty = 500$ km s^{-1}), in which the CIE approximation is good. Both calculations produce very similar cumulative spectra in either the [0, R_s] or [R_s, $2R_s$] region, although the count intensity distributions can differ by as much as a factor of 2 in either the soft or hard X-ray band. On the other hand, the assumption of CIE in the inner region is poor for $\dot{M}_0 = 1 \times 10^{-4}$ M$_\odot$ yr^{-1} and $V_\infty = 2000$ km s^{-1}, which leads to a low central density. Fig. 11 shows clearly that the two ionization calculations produce quite different spectra. Also the soft X-ray count intensity from the CIE calculation is an order of magnitude weaker than that from the non-CIE calculation. This discrepancy is due to the difference in the ionic fraction of the two calculations (Fig. 9). The ionization time scale is longer than the dynamical time scale over which the density drops, so O and Fe are not ionized to as high a degree as specified by CIE at the high central temperature. We refer to this contrast as delayed ionization. Fig. 12 shows
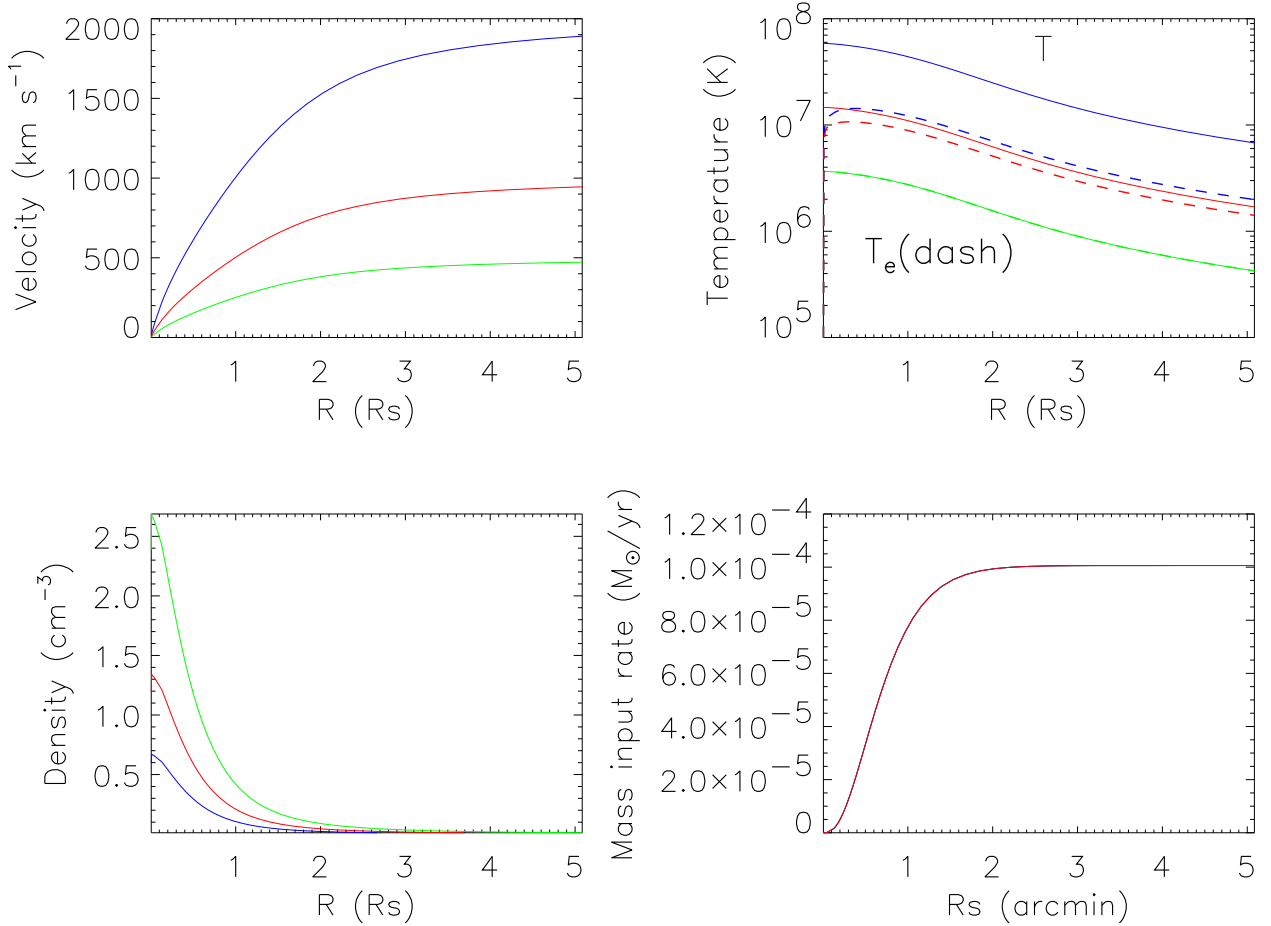
Fig. 8.— Cluster wind profiles for: $V_\infty = 500$ (*blue*), 1000 (*red*), and 2000 (green) km s^{-1}. The mass injection rate is the same ($\dot{M}_0 = 10^{-4}$ M$_\odot$ yr^{-1}). The non-equilibration electron temperature (T_e) in each case is plotted separately (dash lines).

the spatial dependence of the ionic fraction weighted by $n^2 R^2$ pertinent to the calculation of the cumulative spectrum, and compares the CIE and non-CIE spectra at $R = 0.5\ R_s$, where the largest contribution to the cumulative spectrum for $[0,\ R_s]$ comes from. Clearly, much stronger OVII, OVIII lines and Fe-L complex show up in the non-CIE spectrum. They contribute to the soft X-ray excess seen in Fig. 11.

In the outer region, specifically $[2R_s,\ 4R_s]$, the density has decreased so much from spherical expansion that the CIE assumption is clearly not valid in any of the six wind profiles studied. The contrast between the non-CIE and CIE spectra then depends on how far the temperature drops below $\sim 3 \times 10^6$ K, when OIX ions begin to recombine. The more rapidly the temperature decreases with radius, the more the ionization structure deviates from the CIE result. Fig. 13 compares the CIE and non-CIE spectra in the $[2R_s,\ 4R_s]$ region. While the two spectra are quite similar in the

$V_\infty = 2000$ kms^{-1} case, the non-CIE spectrum in the $V_\infty = 500$ kms^{-1} case clearly produces a stronger hard X-ray flux from a saw-tooth-like recombination continuum. The left panel of Fig. 14 compares Oxygen ionic fractions between CIE and non-CIE calculations. In the outer region (e.g., $r = 3.2R_s$), OIX, which produces O^{+7} recombination edges and cascade lines, is absent in the CIE but present in the non-CIE calculation. The right panel of Fig. 14 clearly shows the corresponding spectral differences in the two calculations.

Fig. 15 shows the dependence of the cumulative X-ray luminosity on the mass input rate and wind velocity. The large discrepancy (up to almost one magnitude) between the CIE and non-CIE calculations happens for the high V_∞ and low $\dot{M}_0$ combination, i.e., at a high ratio of energy to mass input rate. In addition, the slope dependence is exactly 2 in the CIE calculation in which the cooling function Λ depends only on the local temperature and density. At a fixed V_∞, the temperature distribution is insensitive to $\dot{M}_0$, so $L \propto \Lambda n^2 \propto \dot{M}_0^2$. In the non-CIE case, however, Λ depends on the evolutionary history of the ionization structure; the slope varies from 2 for $V_\infty = 500$ km s^{-1}, in which the CIE approximation is valid, to ~ 1.3 for $V_\infty = 2000$ km s^{-1}.

The above analysis indicates that the ionization structure is intimately related to the dynamical evolution. CIE is a fair approximation only for the case of a low ratio of energy to mass input rate. Some other processes not considered in our model might weaken/strengthen the non-CIE effect for the stellar cluster wind scenario. For example, outflows from protostars present in a cluster can be regarded as a mass loading process. In this case, the total mass input rate and the density will increase. As shown in SH03, the velocity and temperature will decrease instead, which causes a lower ratio of energy to mass input rate.

Our model may also be applied to galactic superwinds. X-ray emission from strong superwinds may be detectable at very larger radii, where delayed recombination becomes important. But in this case, radiative cooling may not be neglected. Theoretical recombination spectrum has been shown in modelling galactic wind/outflow for the local starburst galaxy NGC3079 (Breitschwerdt 2003).
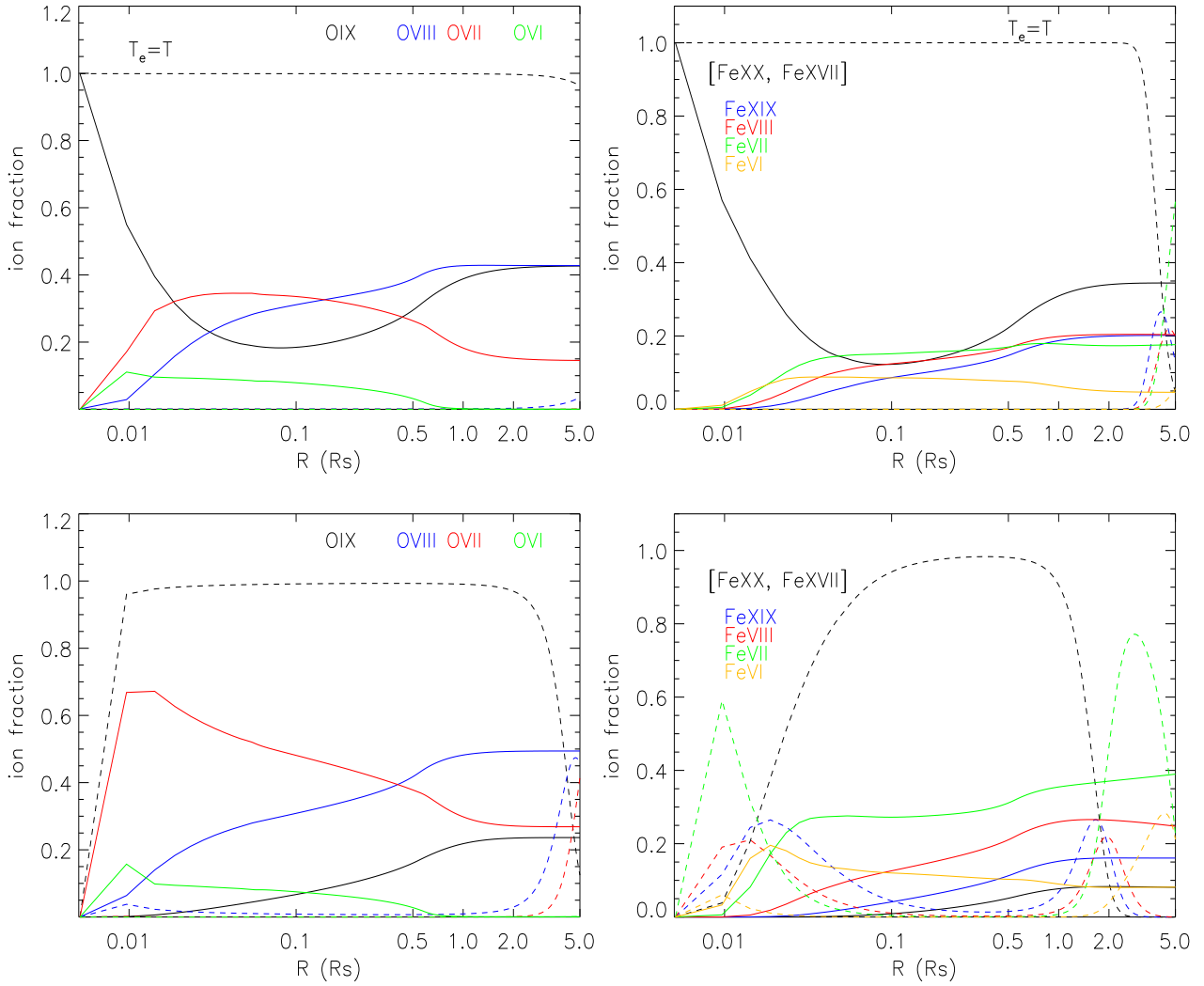
Fig. 9.— Comparison of the ion fractions between the CIE (dash) and the non-CIE (solid) calcula-tions of the cluster wind with $\dot{M}_0 = 1 \times 10^{-4}$ M$_\odot$ yr^{-1} and $V_\infty = 2000$ km s^{-1} for $T_e = T$ (upper row) and T_e calculated via Coulomb interaction (bottom row).
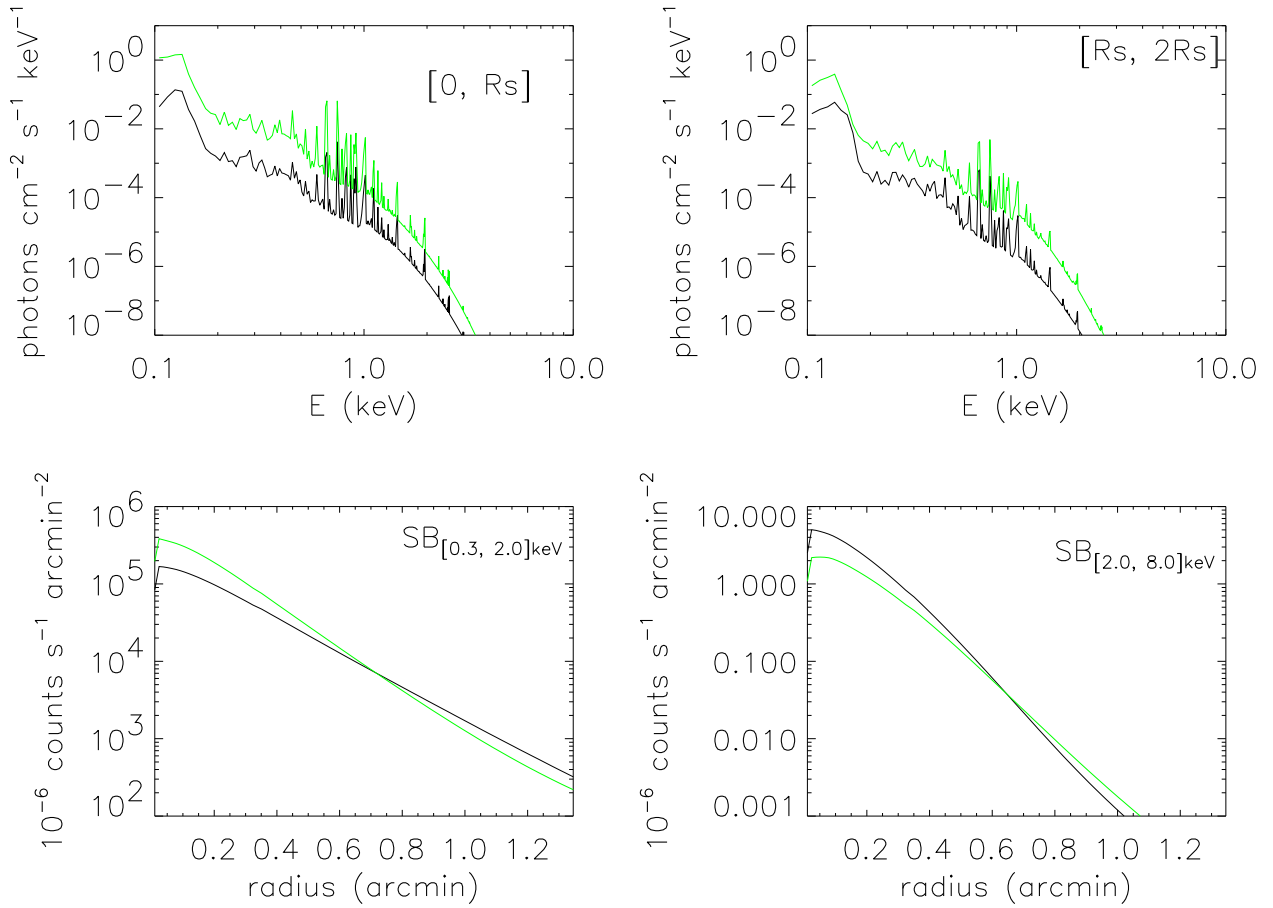
Fig. 10.— Non-CIE model predictions (green), compared with CIE calculations (black) for the wind profile with $V_\infty = 500$ km s^{-1}, as illustrated in Fig. 8. Upper panel: Cumulative spectra within annuli $[0, R_s]$ (right) and $[R_s, 2R_s]$ (left); for clarity, each cumulative spectrum from non-CIE calculations has been increased by a factor of 10. Lower panel: *Chandra* ACIS-S count intensity distributions in $[0.3, 2.0]$ keV (right) and $[2.0, 8.0]$ keV (left) bands.
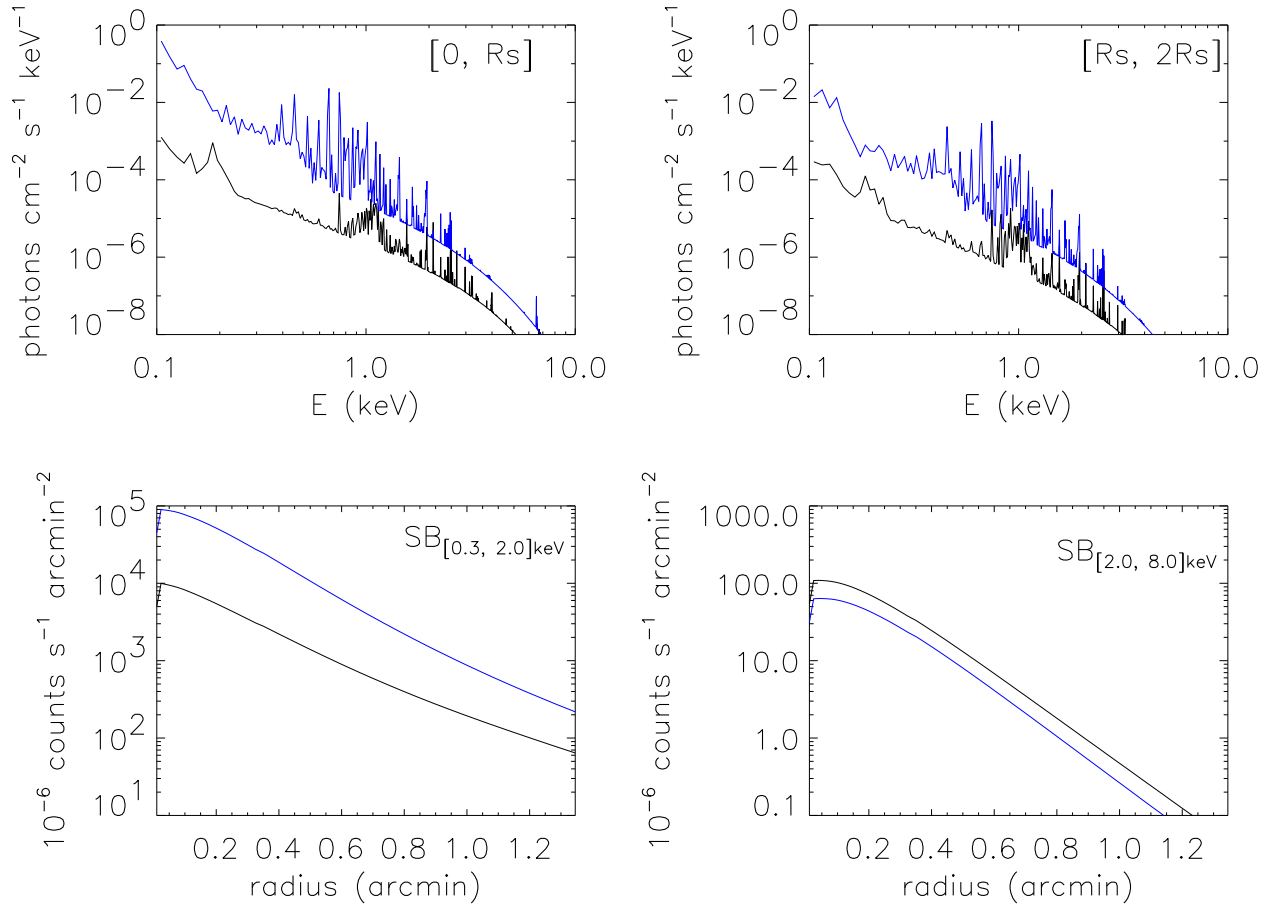
Fig. 11.— Same as Fig. 10 but for the wind profile with $V_\infty = 2000$ km s^{-1} , as illustrated in Fig. 8.
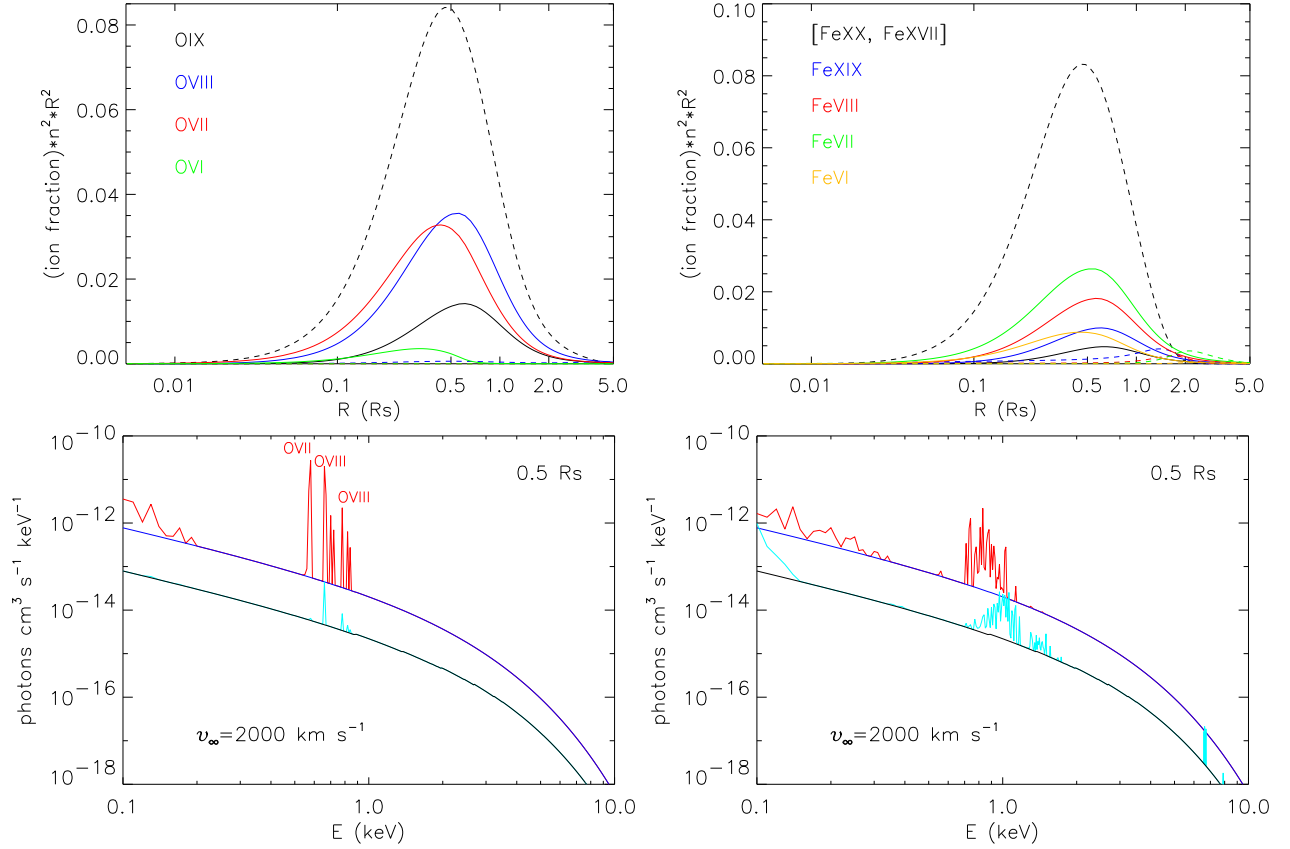
Fig. 12.— Upper panel: Overall spectral contributions as a function of radius for Oxygen ions (left) and Fe ions (right) in the CIE (dash lines) and non-CIE (solid lines) scenarios. Lower panel: Comparison between the spectral contributions from Oxygen (left) and Fe (right) plus the total continuum (black) at $R = 0.5R_s$: CIE (black + cyan) and non-CIE (blue+red). For clarity, the non-CIE spectra have been multipled by a factor of 10. All are based on the wind profile as in Fig. 11.
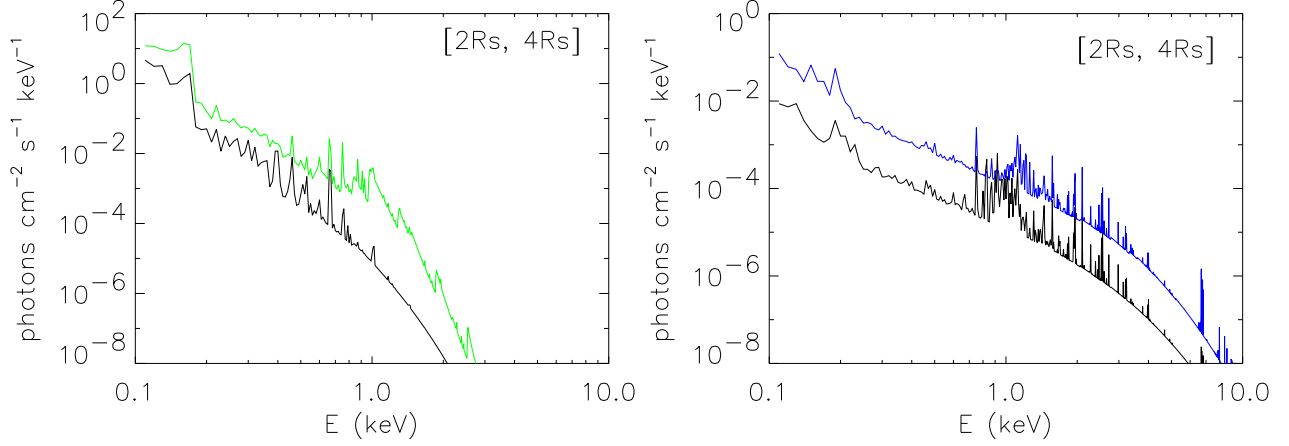
Fig. 13.— Cumulative spectra of the cluster wind with $\dot{M}_0 = 10^{-3}$ $M_\odot$ yr^{-1} and $V_\infty = 500$ (left panel, green) or 2000 (right panel, blue) km s^{-1}. For comparison, the corresponding CIE calculations (black) are also shown. For clarity, each non-CIE spectrum has been multipled by a factor of 10.
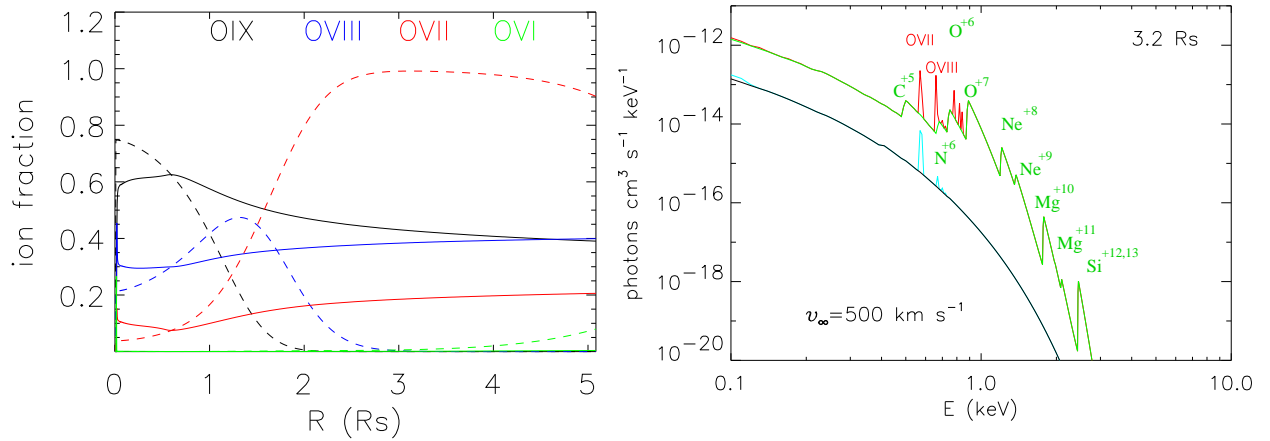

Fig. 14.— Left panel: Comparison of the Oxygen ionic fractions between the CIE (dash) and non-CIE (solid) calculations of the cluster wind with $\dot{M}_0 = 1 \times 10^{-3}$ $M_\odot$ yr^{-1} and $V_\infty = 500$ km s^{-1}.. Right panel: Similar to the lower left panel of Fig. 12 but at 3.2 R_s. Free-bound recombination edges are denoted by the contributing ions (green).
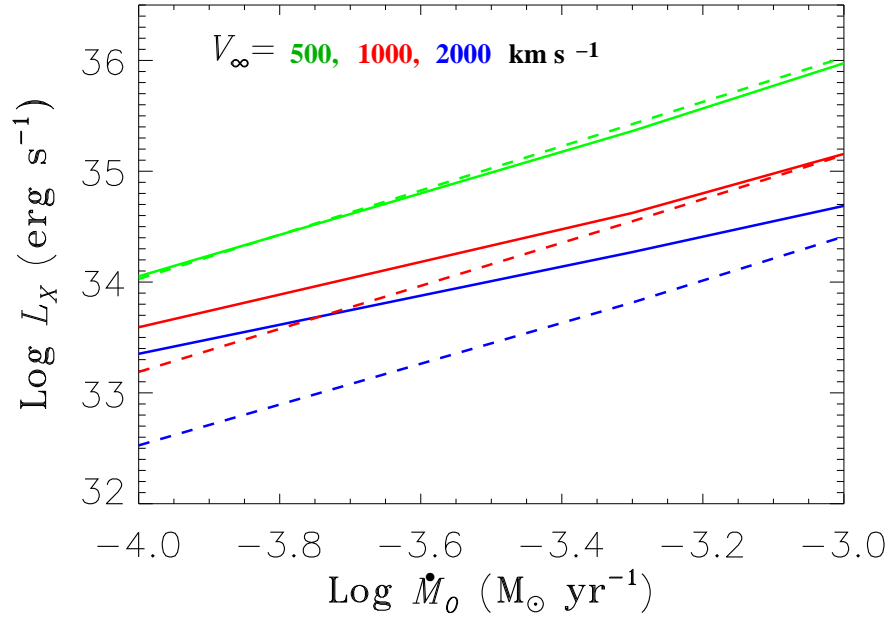
Fig. 15.— CIE (dash) and non-CIE (solid) calculations of the cumulative X-ray luminosity versus mass input rate. An exponential stellar mass distribution with $R_s = 1.97$ pc and $V_\infty = 500$ (green), 1000 (red), and 2000 (blue) km s^{-1} is studied.

5. APPLICATION TO NGC 3603

NGC 3603 at a distance of 7 kpc is the most luminous giant HII region in the Galaxy (e.g., Moffat et al. 1994). The star cluster responsible for the HII region is regarded as a Galactic analogue to SSCs observed in other galaxies. With an age of less than 3 Myr (Sung & Bessell 2004), the cluster contains massive stars as well as low-mass pre-main sequence (PMS) stars.

Stars in NGC 3603 have been investigated from near-infrared to X-ray (e.g., Sung & Bessell 2004; Moffat et al. 2002). Based on 44 spectroscopically classified stars, which dominate the mass and energy injections, SH03 estimate the total mass input rate from the cluster as $\dot{M}_0 = 2.3 \times 10^{-4}$ M$_\odot$ yr^{-1} and the mean weighted stellar wind terminal velocity as $V_\infty = 2844$ km s^{-1}. We use the observed diffuse X-ray emission of NGC 3603 to test our NEI model of stellar cluster winds.

5.1. Data Analysis

We use the *Chandra* ACIS-I observation of NGC 3603 (observation ID 633), which was taken in May, 2000 for an exposure of 50 ks. Moffat et al. (2002) used this observation to study primarily discrete X-ray sources, although they also characterized the remaining "diffuse" emission with a one-temperature CIE thermal plasma model. Here, we concentrate on the diffuse emission.

We reprocess the ACIS-I event data, using the *Chandra* Interactive Analysis of Observations software package (CIAO, version 3.2). This reprocess, including the exclusion of time intervals with background flares, results in a net 47.4 ks exposure (live time) for subsequent analysis.

The superb spatial resolution of the data allows for the detection and removal of much of the X-ray contribution from individual stars. We search for X-ray sources in the 0.5-2, 2-8, and 0.5-8 keV bands by using a combination of three source detection and analysis algorithms: wavelet, sliding-box, and maximum likelihood centroid fitting (Wang 2004). Source count rates are estimated with the 90% energy-encircled radius (EER) of the point spread function (PSF). The accepted sources all have the local false detection probability $P \leq 10^{-6}$. The right panel of Fig. 16 shows the detected point sources within the cluster field. The source detection in the inner $\sim 20''$ radius of the cluster is highly incomplete due to severe source confusion.

To analyze the remaining "diffuse" emission from the cluster, we remove the detected source regions from the data. For each faint source with a count rate (CR) ≤ 0.01 counts s^{-1}, we exclude a region of twice the 90% EER, which increases with off-axis angle. For each source with CR > 0.01 counts s^{-1}, an additional factor of $1 + \log(\mathrm{CR}/0.01)$ is multiplied to the source-removal radius to further minimize the residual contribution from the PSF wings of relatively bright sources.

We extract the spectra of the diffuse X-ray emission separately from the two annular regions, Da and Db (divided to contain roughly the same number of counts), as well as an accumulated point
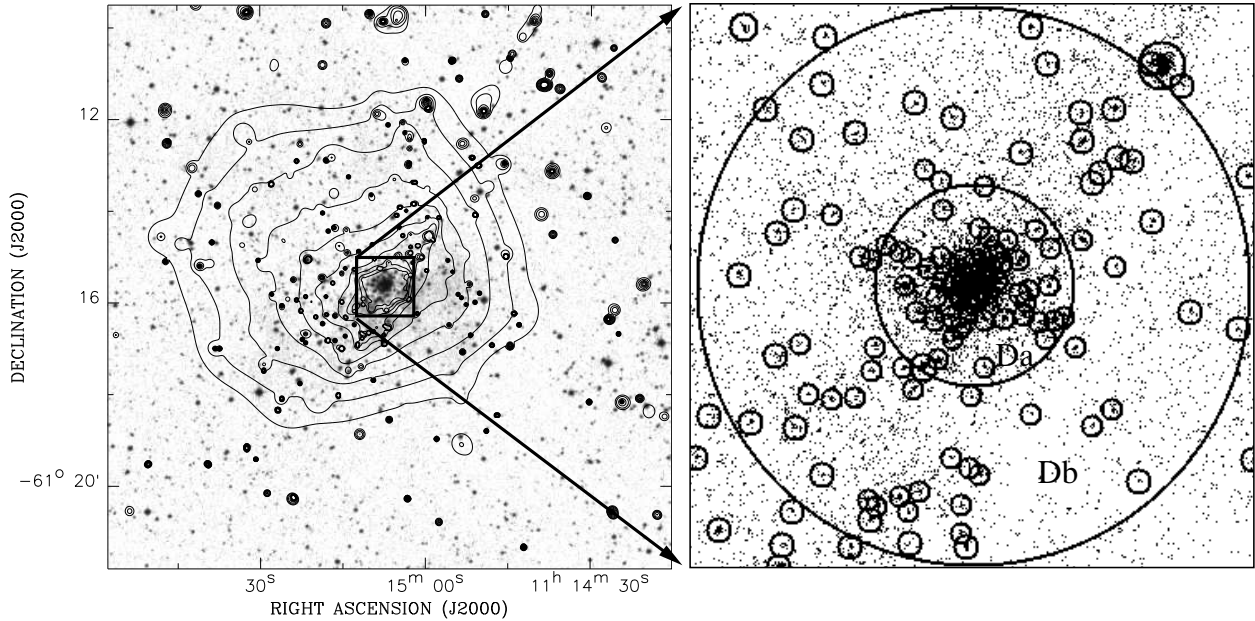
Fig. 16.— *Chandra* ACIS-I observation of NGC 3603. Left panel: The 0.5-8.0 keV intensity contours (at 52, 58, 70, 94, 130, 178, 238, 310, 394, and 490 $\times10^{-4}$ counts s^{-1} arcmin^{-2}) overlaid on an optical image. Right panel: A close-up of the central cluster. The image shows the ACIS-I event distribution. Point-like X-ray sources are marked individually with small circles of $2\times$ the PSF 90% EER. The two annulii, Da ([$19''$, $30''$]) and Db ([$30''$, $83''$]), are used to extract the spectra of the diffuse emission.

source spectrum from the combined region (Da+Db). An additional spectrum extracted from the outer annulus between $4'.0$ and $5'.0$ radii is used as the local background of the diffuse X-ray emission, which in turn are normalized for the background subtraction of the sources. Fig. 17 shows a joint-fit of the spectra with our cluster wind model plus a thermal model, which is used to characterize the point-like source spectrum. Here we assume that the detected and undetected point sources have the same spectral shape. We jointly fit the diffuse spectra and the accumulative spectrum of point sources together. We find that the spectral fit results are insensitive to the assumed stellar distributions of our model and to the exact scale radius. Therefore, Table 1 includes only the results from the model with the more physical exponential stellar mass distribution; the fixed scale radius $r_{sc} = 0.68$ pc corresponds to the same sonic radius as adopted by SH03. The best-fit model predicts the luminosity contributions of $L_{2-8 \text{ keV}} \sim 2.5 \times 10^{33}$ erg s^{-1} and 8.8×10^{33} erg s^{-1} from the cluster wind and residual point-like source components. Fig. 18 shows the predicted radial surface intensity distribution of the cluster wind contributions compared with the observed "diffuse" emission in two energy bands.

Table 1. Joint spectral fit results[a]

	Parameter	Model
N_{H}	$(10^{22}\ \mathrm{cm}^{-2})$	$0.81^{+0.06}_{-0.05}$
Cluster wind component		
r_{sc}	(pc)	0.68 (fixed)
Abundance	$(Z_\odot)$	$0.21^{+0.12}_{-0.11}$
$Log\dot{M}_0$	$(\mathrm{M}_\odot\ \mathrm{yr})$	$-3.37^{+0.42}_{-0.24}$
V_∞	$(1 \times 10^3\ \mathrm{km\ s}^{-1})$	1.53 (> 0.50)
Point-like source component		
kT	(keV)	$3.79^{+0.41}_{-0.33}$
K_1[b]	$(10^{-4}\ \mathrm{photons\ cm}^{-2})$	$3.63^{+0.77}_{-1.56}$
K_2[c]	$(10^{-4}\ \mathrm{photons\ cm}^{-2})$	$7.76^{+1.38}_{-1.73}$
K_3[d]	$(10^{-3}\ \mathrm{photons\ cm}^{-2})$	$3.26^{+0.22}_{-0.19}$
χ^2/d.o.f.		301.3/457

[a]Note: all error bars are at the 90% confidence

[b]K_1 is the MEKAL normalization of the undetected point sources in Region Da.

[c]K_2 is same as K_1, but in Region Db.

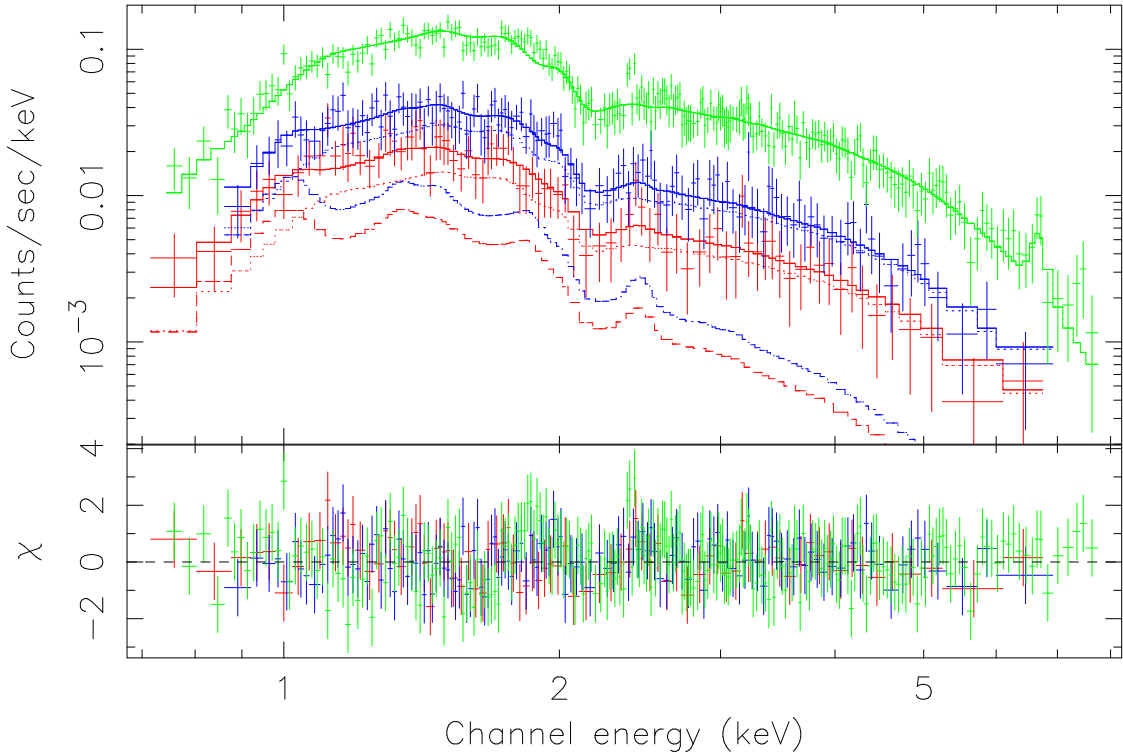[d]K_3 refers to the MEKAL normalization of the detected point sources.

Fig. 17.— Joint fit to the spectra of the point-like sources (green) and the two diffuse X-ray spectra (red and blue) of NGC 3603. All these spectra are grouped to contain at least 25 net counts per bin. The point-source spectrum is modelled with an optically-thin thermal plasma, while the diffuse X-ray spectral model also contains a joint-fitted residual point-like source contribution (dotted histograms) as well as the cluster wind component (dashed).

5.2.   Discussion

The above results represent the first quantitative comparison of a self-consistent NEI cluster wind model with observational data. Our fitted foreground X-ray-absorbing gas column density, $N_H = 8.1^{+0.6}_{-0.5} \times 10^{21}$ cm^{-2}, is consistent with the interstellar reddening toward NGC 3603. The reddening of $E(B-V) = 1.25 - 1.8$ mag, determined by Sung & Bessell (2004) from 115 bright stars in the field, corresponds to $N_H = (7.3 - 10.4) \times 10^{21}$ cm^{-2} (e.g., Bohlin et al. 1978). The derived abundance of the wind is sub-solar: $Z = 0.21^{+0.12}_{-0.11}$ $Z_\odot$. This abundance likely represents an underestimate of the true value due to the oversimplification in the 1-D model, which does not account for substructures in both temperature and density. Such substructures lead to smearing out of spectral line features that characterize the metal abundance. Our fitted mass input rate and terminal velocity of the cluster wind is, within a factor of ~ 2, consistent with the empirical estimation by SH03 (§5). But the cluster wind contributes only about 25% of the observed total diffuse emission luminosity.
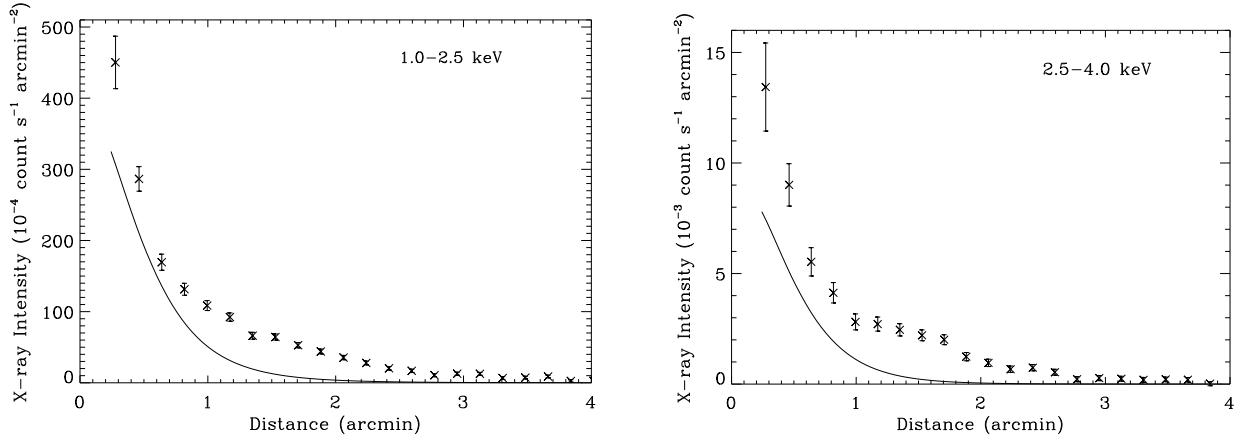
Fig. 18.— ACIS-I intensity profiles of the diffuse X-ray emission (crosses with 1σ error bars) in the 1.0-2.5 keV (left) and 2.5-4.0 keV (right) bands. The solid lines represent the predicted cluster wind contributions based on the spectral fit.

While the remaining of the diffuse emission likely originate from undetected point-like sources, what is their nature? Moffat et al. (2002) and Sung & Bessell (2004) suggested that PMS young stellar objects (YSOs) may be responsible. According to the study by Saga et al. (2001), the NGC 3603 cluster has an initial mass function (IMF) that can be characterized by a power law with a slope of 0.84 and contains about 2×10^2 stars in the mass range 7-75 $M_\odot$. Using this IMF, we estimate the presence of about 8×10^3 YSOs (0.3-3 $M_\odot$) in this cluster. The study of such YSOs in the Orion Nebular (Feigelson et al. 2005) shows that their average 2-8 keV luminosity is $\sim 1 \times 10^{30}$erg s^{-1} per star. Thus the expected total YSO contribution in the NGC 3603 cluster is $L_{2-8 \text{ keV}} \sim 8 \times 10^{33}$, consistent with the prediction from our spectral fit.

6. SUMMARY

In this paper, we have presented a NEI spectral code, which is based on our updated atomic data, including the atomic process of recombinations into highly excited levels. We have shown important differences between the CIE and non-CIE calculations.

We have constructed a self-consistent physical model for super stellar cluster winds, combining the NEI code with a 1-D steady-state adiabatic wind solution. We find that in the inner region of the star cluster, the NEI effect is significant in the regime of a high energy to mass input ratio and manifests in an enhanced soft X-ray emission, which could be an order of magnitude more luminous than that obtained under the CIE assumption.

We apply the cluster wind model to the *Chandra* data on NGC 3603 and find that the inferred mass and energy input rates of the stellar cluster winds are comparable to the empirical estimates. But the cluster wind in NGC 3603 accounts for no larger than 50% of the total diffuse X-ray

emission. YSOs are likely responsible for the remaining diffuse emission.

REFERENCES

Allen, C.W. 1973, Astrophysical Quantities

Arnaud, M., & Rothenflug, R. 1985, A&AS, 60, 425

Arnaud, M., & Raymond, J. 1992, ApJ, 398, 394

Bohlin, R.C., Savage, B.D., & Drake, J.F., 1978, ApJ, 224, 132

Borkowski, K.J., Sarazin, C.L., & Blondin, J.M. 1994, ApJ, 429, 710

Borkowski, K.J., Lyerly, W.J., & Reynold, S.P. 2001, ApJ, 548, 820

Breitschwerdt D., Egger, R., Freyberg, M.J., Frisch, P.C., Vallerga, J.V. 1996, Space Sci. Rev., 78, 183

Breitschwerdt D., & Schmutzler, T. 1999, A&A, 347, 650

Breitschwerdt D. 2003, Rev.Mex.Astron.Astrof.Ser.Conf. 15, 311

Cantó J., Raga A. & Rodríguez L. 2000, ApJ, 536,896

Chevalier R, & Clegg A., 1985 Nature, 317, 44

Dere, K.P., Landi, E., Young, P.R., DeL Zanna, G. 2001, ApJ, 134, 331

Dopita, M.A., Sutherland, R.S., Schweiger, G.S. 2002, Astrophysics of the Diffuse Universe , Berlin, New York: Springer.

Feigelson, E.D., Getman, K., Townsley, L., et al. 2005, ApJS, 160, 379

Gorczyca, T.W., Kodituwakku, C.N., Korista, K.T., Zatsarinny, O. 2003, ApJ, 592, 636

Gu, M.F. 2003, ApJ, 582, 1241

Heckman, T. M., Armus, L., & Miley, G. K. 1990 ApJS, 74, 833

Kaastra, J.S., & Mewe, R. 1993, A&AS, 97, 443

Karzas, W.J., & Latter, R. 1961, ApJS, 6, 167

Kudritzki, R. & Puls, J. 2000, ARA&A, 38, 613

Law, C., & Yusef-Zadeh, R. 2004, ApJ, 611,858

Mazzotta, P., Mazzitelli,G., Colafrancesco S. Vittorio N. 1998, A&AS, 117 , 920 (**Mazz98**)

Mewe, R., & Cronenschild, E.H.B.M. 1981, A&AS, 45, 11

Mewe, R. 1997, in *X-ray spectroscopy in Astrophysics*, eds. J. van Paradijs, Bleeker J.A.M., Lectrure Notes in Physics, 520, 109

Moffat, A.F.J., Drissen, L., & Shara, M.M. 1994, ApJ, 436, 183

Moffat, A.F.J., Corcoran, M.F., Stevens, I.R., et. al 2002, ApJ, 573, 191

Nahar, S.N. in *Atomic Data Needs In X-Ray Astronomy*, 2000, ed. M.A. Bautista, T.R., Kallman, & A.K. Pradhan (NASA/CP-2000-209968), 75

Osterbrock, D.E. 1989, Astrophysics of Gaseous Nebulae and Active Galactic Nuclei

Raga A.C., Velázquez, P.F., Cantó J., Masciadri, E. Rodríguez L.F. 2001 ApJ, 559, L33

Rockefeller, G., Fryer, C.L., Melia, F., Wang, Q.D. 2005, ApJ, 623, 171

Saga, R., Munari, U., de Boer, K.S. 2001, MNRAS, 327, 23

Stevens, I.R., & Hartwell, J.M. 2003 MNRAS, 339, 280 (**SH03**)

Strickland, D.K., & Stevens, I.R. 1999, MNRAS, 306, 43

Strickland, D.K., Heckman, T.M., Weaver, K.A., Hoopes, C.G., & Dahlem, M. 2002, ApJ, 568, 689

Sung, H., & Bessell, M.S. 2004, AJ, 127, 1014

Sutherland, R.S., & Dopita, M.A. 1993, ApJS, 88, 253

Verner, D.A., & Yakovlev, D.G. 1995, A&AS, 109, 125

Verner, D.A., & Ferland, G.J. 1996, ApJS, 103, 467

Wang, Q.D. 2004, ApJ, 612, 159

Wang, Q.D., Dong, H., & Lang, C. C. 2006, MNRAS, submitted

Whitmore, B. 2000, STScI Symposium Series 14, ed. M. Livio, astro-ph/0012546

Young, P.R., Del Zanna, G., Landi, E., Dere, K. P., Mason, H. E., & Landini, M. 2003, ApJS, 144, 135

Yusef-Zadeh, F., Law, C., Wardle, M., Wang, Q. D., Fruscione, A., Lang, C. C. , Cotera, A. ApJ, 570, 665